LA-UR-03-2105

Approved for public release; distribution is unlimited.

43

c.1

Title: A COMPACT LAYOUT FOR A 50 GeV PROTON RADIOGRAPHY FACILITY

Author(s): Filippo Neri, LANSCE-1 C. Thomas Mottershead,LANSCE-1
Barbara Blind, LANSCE-1 Andrew J. Jason, LANSCE-1
Peter L. Walstrom, LANSCE-1 Martin Schulze, LANSCE-AHF
Lawrence J. Rybarcyk, LANSCE-1 Tai-Sen F. Wang,
LANSCE-1 Ben Pritchard, LANSCE-AHF David Johnson,
LANSCE-AHF H. Arch Thiessen, LANSCE-AHF
Pat Colestock, LANSCE-AHF

Submitted to: American Nuclear Society Conference

Los Alamos
NATIONAL LABORATORY

A Compact Layout for a 50 GeV Proton Radiography Facility

Filippo Neri, Tom Mottershead, Barbara Blind, Andrew Jason,
Peter Walstrom, Larry Rybarcyk, Tai Sen Wang
Los Alamos National Laboratory, LANSCE-1
Ben Pritchard, David Johnson, Arch Thiessen, Pat Colestock,
Martin Schulze,
Los Alamos National Laboratory, LANSCE-AHF

We describe a new compact layout for a 50 GeV proton radiography facility. The more compact design utilizes two-point extraction from the main ring to drive an optimal 8 view imaging system. The lattice design of both the main ring, and of the corresponding 8.5 GeV booster ring is described. The rings have very good longitudinal stability, which is of interest for other applications of high current proton machines in this energy range.

Introduction to Proton Radiography

Proton radiography is a new technology for imaging the interior of objects that can be penetrated by high-energy protons. A broad beam of high energy protons shines through the object, suffering position dependent nuclear attenuation, making radiographic contrast, multiple Coulomb scattering (MCS) spreading the beam in angle, and energy loss and straggling, spreading the beam in energy. The net effect is that an image is imprinted in the beam by its passage through the object. A magnetic lens extracts the image by refocusing the varied scattering angles onto a detector plane. The performance of the lens is defined by field-of-view and resolution. The Field-of-view (FOV) is defined by the maximum phase space coordinates that will pass through the lens without striking the pipe. The lens is in focus at only one energy. Protons of other energies are out of place when they are detected. This energy dependent blur is called chromatic aberration, and is one of the main limitations on the resolution of the system. Chromatic aberration has two components, coming from the effects of changing energy on the two basis rays of magnetic optics. These are the sinelike ray $S(z)$ which starts on the axis with unit slope, and the cosinelike ray $C(z)$ which starts at unit amplitude with zero slope. Fig 1 shows the family of sinelike and cosinelike rays for the type of lens used in proton radiography. The top row is the x-plane, the bottom row is the y-plane.

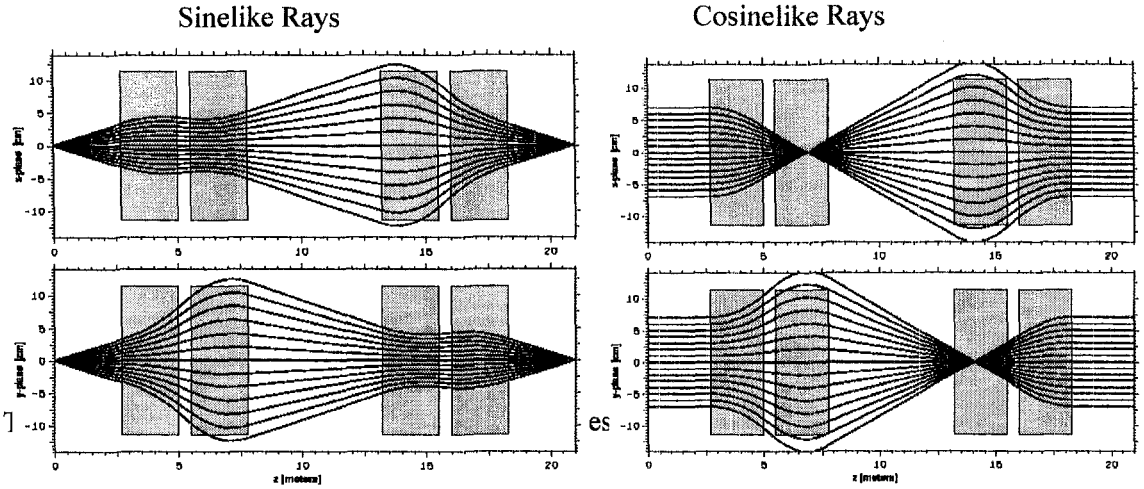

Figure 1: Proton rays in imaging lens.

than nominal energy focus downstream of the nominal focal plane, those of lower than nominal energy focus a bit upstream. This movement of focal plane with energy is described by the main chromatic coefficient C =dR12/dE. The cosinelike rays define the magnification, which expands in one plane and contracts in the other as the energy changes. Both of these chromatic effects can blur the final image, which is the superposition of all the energies in the final beam. Proton radiography, however, eliminates the chromatic magnification blur by using a specially correlated beam to illuminate the object. The design of the lens specifies what this correlation must be.

The general trajectory from initial point is

$$x(z) = x_0 C(z) + \theta_0 S(z)$$

The R-matrix of the lens gives the final coordinates on the image plane:

$$\begin{pmatrix} x \\ \theta \end{pmatrix} = \begin{bmatrix} R_{11} & R_{12} \\ R_{21} & R_{22} \end{bmatrix} \begin{pmatrix} x_0 \\ \theta_0 \end{pmatrix}$$

The final position of a ray is independent of its energy deviation if

$$\frac{dx_f}{d\Delta} = \frac{d}{d\Delta}\left[x_0 R_{11} + \theta_0 R_{12}\right] = x_0 R_{11}' + \theta_0 R_{12}' = 0$$

This is satisfied if $\theta_0 = w x_0$ with $w = -R_{11}' / R_{12}'$

•Proton radiography illuminates the object with such achromatic rays, so the initial angle exiting

$$\theta_0 = wx_0 + \varphi_0$$

the object takes the form with deviation coming from mainly from MCS scattering.

• The final position on the image plane of the general scattered ray is then

$$x_f = R_{11}x + R_{12}(wx + \varphi) + (R_{11}' + wR_{12}')x\Delta + R_{12}'\varphi\Delta + \cdots = -x + (C_x\Delta)\varphi$$

A proton radiography facility consists of a diffuser to increase the beam divergence, an illuminator matching section to expand the beam to cover the object while producing the required phase space correlation at the object, and two sequential imaging lenses to focus the scattered protons onto fluorescent glass screens in two locations, thereby forming a visible light images to be recorded by a set of gated TV cameras . Fig. 2 shows the single lens version of the system currently operational at Brookhaven National Laboratory. This 24 GeV system is a prototype of the proposed AHF system.

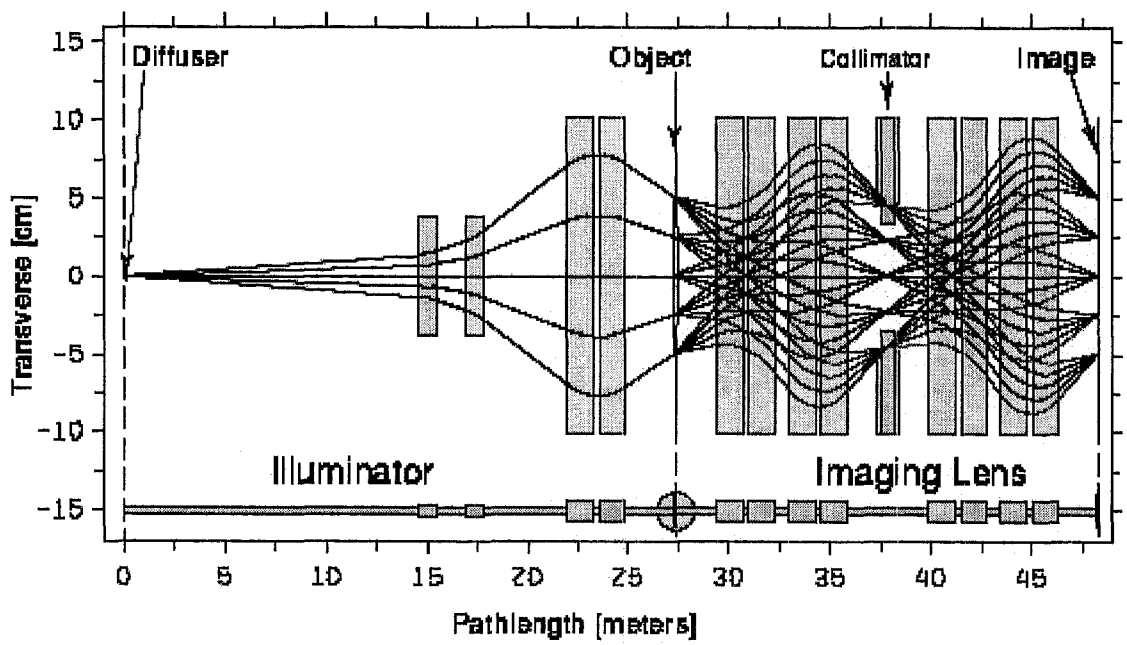

Figure 2: Example of PRAD lens system.

Intensity Requirements and Intensity Limits

We require that for each beam axis, there are 1x10^11 protons delivered to the beam diffuser in each bunch. Assuming 12 axes, 20% beam losses in beam splitters, and allowing a 30% safety factor, we require 2^12 protons per bunch delivered at the output of the main ring. In a main ring containing 24 bunches, this requires 5x10^13 protons per accelerator cycle.

There are beam losses in all accelerators. Since such losses are difficult to compute, we have assumed some arbitrary loss allowances at each stage in the acceleration, as shown in Fig. 3. The main point of this figure is to show the (per bunch) beam intensity requirement versus location in the acceleration cycle as expected using our arbitrary beam loss allowances.

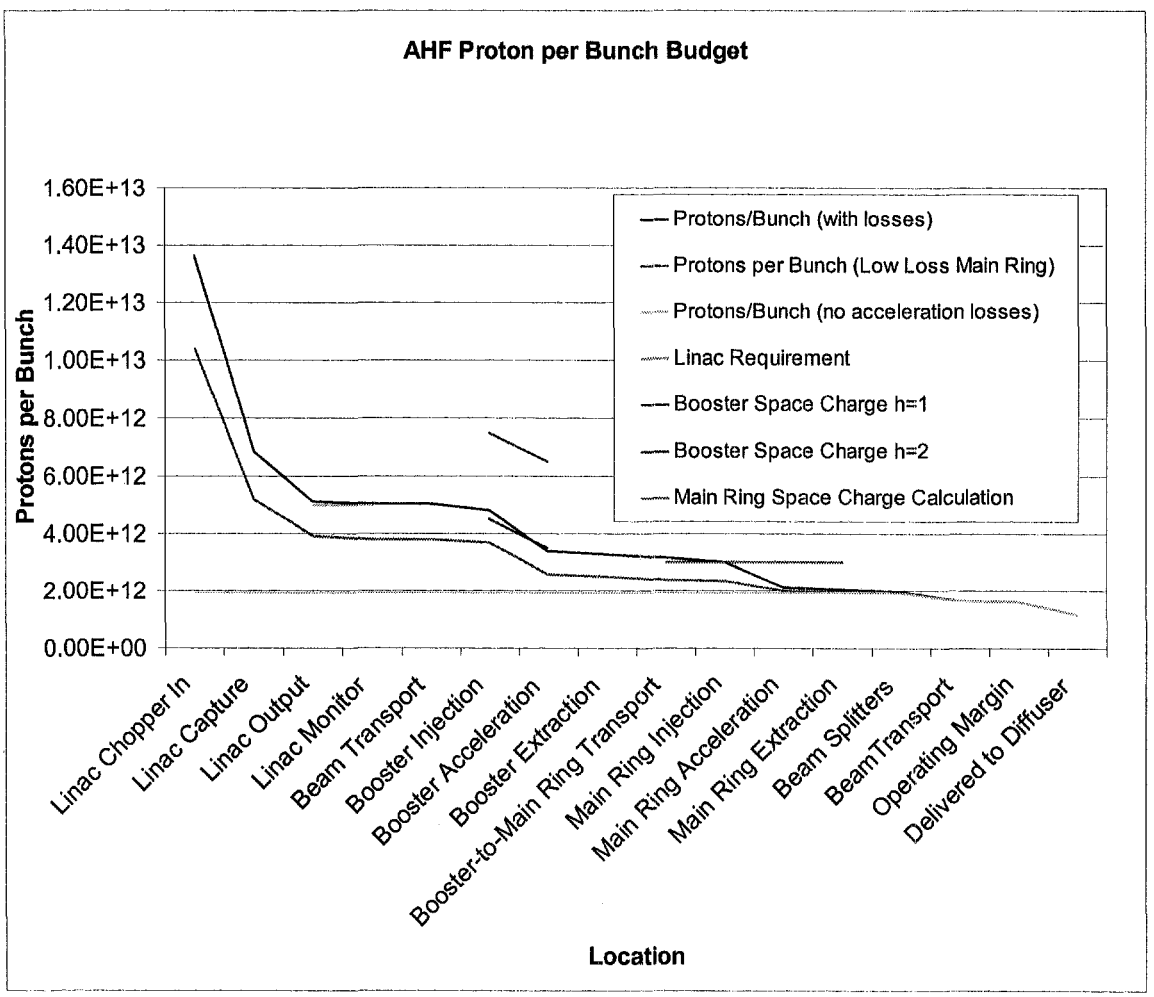

Figure3: Proton budget in AHF system.

We assume that in the synchrotrons, there are two processes that limit the intensity. The first is the space charge limit, which occurs shortly after injection in each synchrotron. The second limit results from collective beam instabilities. We arbitrarily assume that the beam instability limit is given by the Keil-Schnell criterion for longitudinal microwave instability. The Keil-Schnell limit is lowest (most limiting) at the time of the end of acceleration in each synchrotron, and also limits intensity at transition crossing time if we cross transition in the synchrotron. We have shown the

maximum beam available in the space charge limited regime as calculated with program SIMPSONS on Figure A, showing that the accelerator design for AHF has the capability to deliver the required beam intensity even in the presence of beam losses. In Fig. 4, we show the Keil-Schnell limit vs. beam energy in the several designs considered for AHF.

No completely satisfactory treatment of beam stability limits exists for crossin transition. In a synchrotron, although some limits have been given. Typically, the state-of-the-art allows for a fewx10^13 protons per cycle when crossing transition. We assume that AHF will be "worse" than other existing machines due to the slow ramp rate, and have not indicated a "stable" beam intensity limit in Fig. 4.

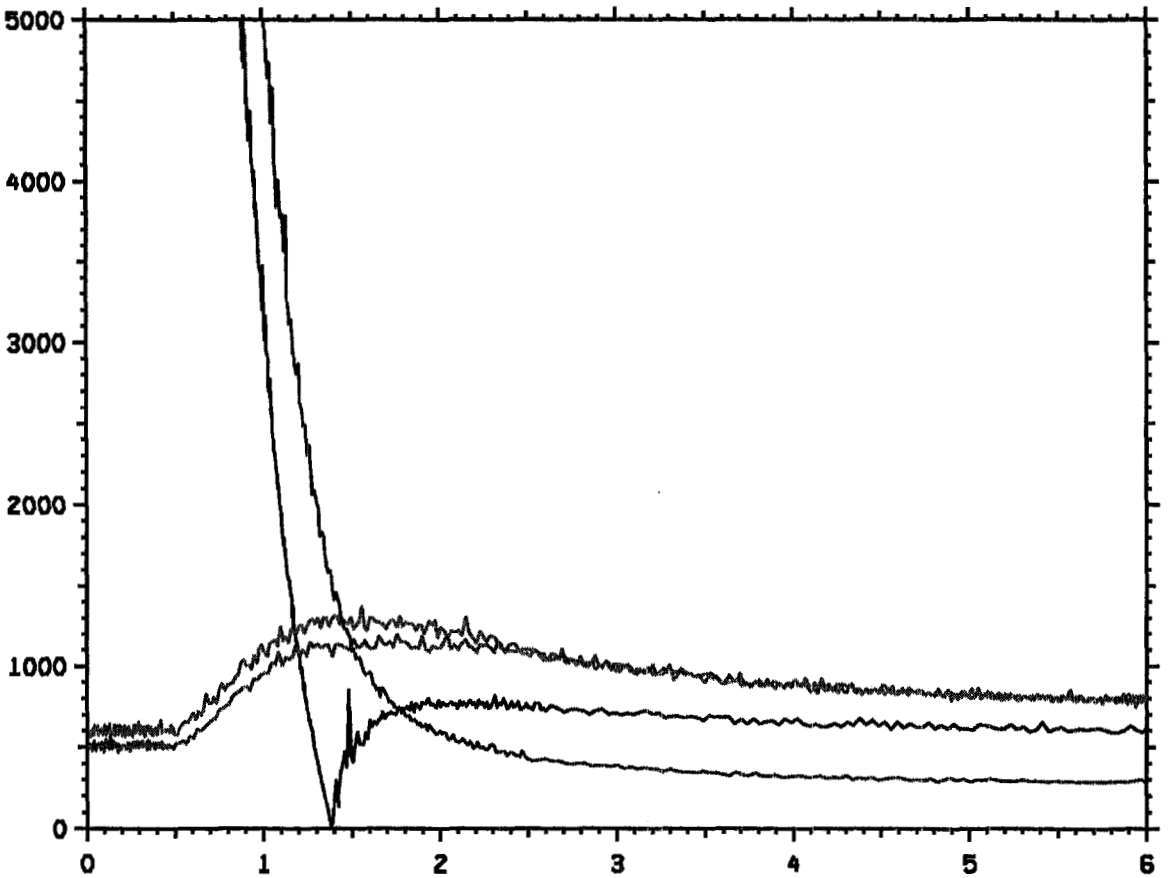

Figure 4: Stability limits for different 50-GeV main rings.

From an examination of Fig. B, one can see why we prefer the solution of a "higher energy booster" that injects a main ring above its transition energy – thus avoiding transition crossing altogether, and a main ring with low transition energy, which has the highes available Keil Schnell limit near its maximum energy. There are several other reasons to prefer a low transition energy main ring that are not discussed here.

New Low-Transition-Gamma Synchrotron Lattices

The intended application of the 50 GeV proton synchrotron (main ring) in the AHF context requires robust, stable and highly reliable operation as well as operational flexibility. Principal design criteria call for a simple lattice of conventional and conservative design. Operational simplicity means few adjustable parameters, and economical installation requires repetitive cell

structures involving few types of identical, room-temperature magnets. The main ring lattice must incorporate at least 3 dispersionless straight sections of sufficient length to accommodate fast kick-injection of 4 GeV protons, 0.2 MV of RF cavities, and single-bunch fast-extraction as well as the future option of slow-spill extraction.

Two additional possible lattice structures are being considered for the main ring. The principal feature separating these two lattices from the previus ones is the transition energy. The transition gamma of the new lattices is 9.2 or 9.4. Both lattices are conventional, regular FODO lattice designs. Such a low transition gamma allow to inject above the transition energy from a booster capable of a top energy of 8.5 GeV (kinetic energy.)

Triangular Lattice

The main ring layout of the first of the two lattices is presented in Figure 6.

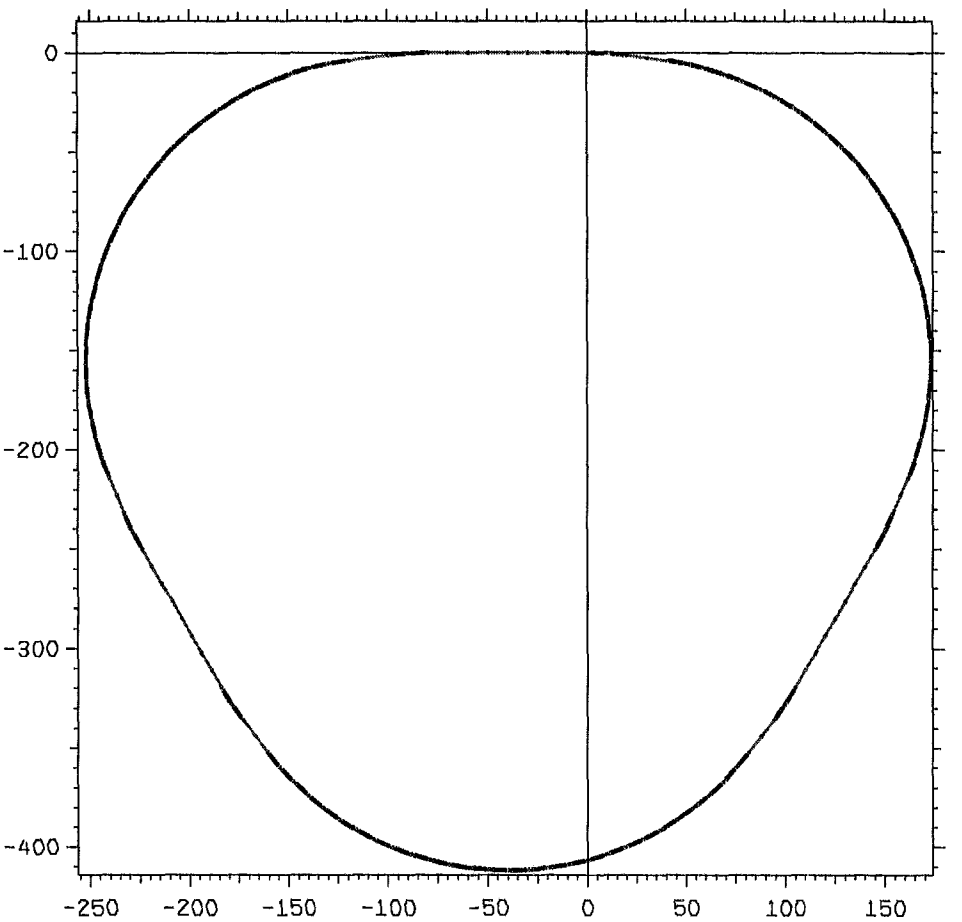

Figure 6: Layout of the triangular version of the low-transition-gamma 50 GeV main ring lattice.

]

This conventional 3-sided ring geometry employs a regular FODO focusing structure repeated throughout the ring, in both arc and straight sections, for a total of 66 identical cells of 56.8°/56.6° horizontal/vertical phase advance each. The three identical 60°-bend arc sections each consist of 18 cells filled with 32 full-length dipole magnets (6.78 m long, maximum gap field 1.64 T at 50

GeV), and 2 dispersion-suppressing cells before each arc end with no dipoles. A single family of 132 identical quadrupole magnets (1.0 m long) is employed. A FODO cell length of 20.0 m results in a ring circumference of 1320 m. Four cells form each of the three 80 m-long straight sections. The result is a symmetric ring of superperiodicity 3.

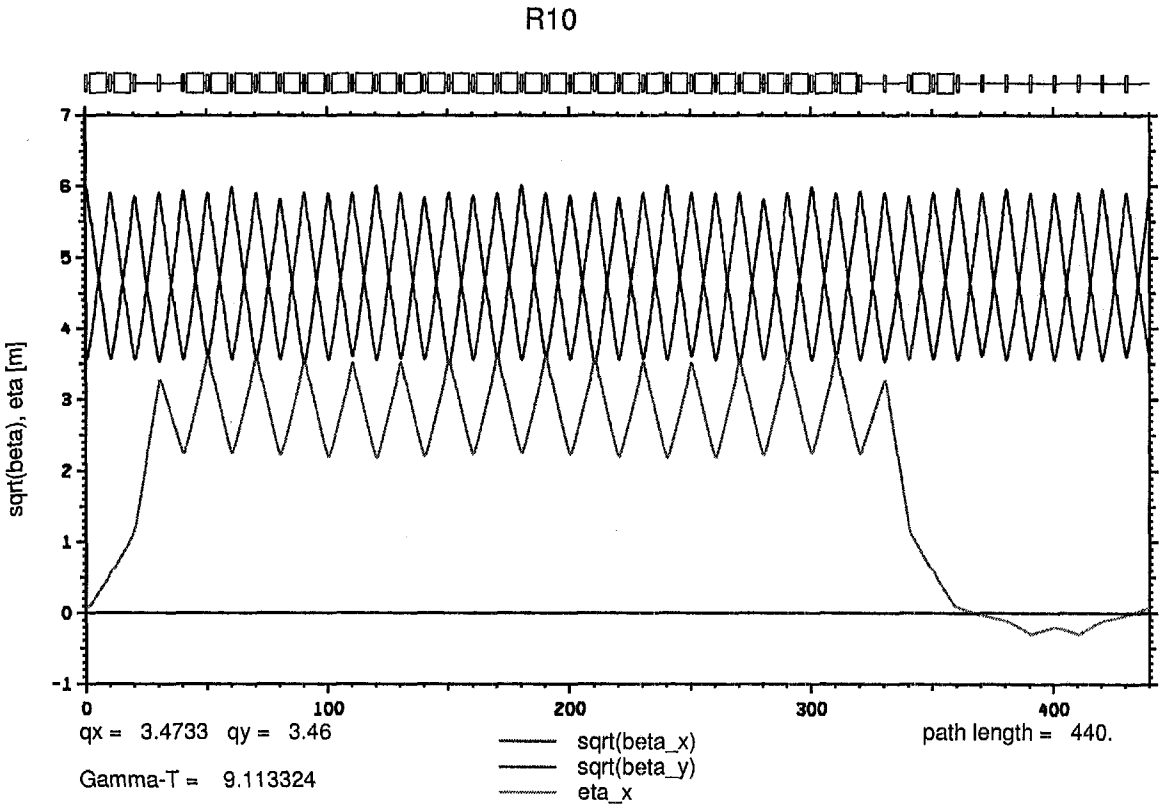

[Figure 7: Lattice functions of the triangular lattice in one superperiod (1/3 ring)]

As illustrated in Figure 7, this very simple, straightforward lattice is characterized by perfectly smooth lattice functions around the ring: no modulation of the 36 m maximum betatron amplitude, and a uniform dispersion amplitude of 3.6 m within the arcs. The latter produces a real transition-energy γ-factor of 9 (corresponding to about 8 GeV transition energy). Longitudinal dynamics simulations for this lattice [cf. Longitudinal Dynamics section] have shown that the beam appears to pass through transition with acceptably small beam loss and emittance growth, whit only fast RF phase jump at transition. But the present design also allows for the later addition of a booster capable of an extraction energy of over 8.5 GeV as an upgrade option if needed for higher intensity operation with very low losses.

The ring betatron tunes of $Q_x = 10.42$, $Q_y = 10.38$ in the present design place the nominal working point in betatron tune space in a region free of systematic and structural sum resonances (see Figure 8). Because of negative tune shifts from beam space charge, the working point is located below the octupole coupling resonance $2\upsilon_x - 2\upsilon_y = 0$, but since the horizontal and vertical tunes are essentially unsplit, some emittance growth is possible in the presence of strong space charge forces. The tunes per superperiod also are somewhat close to (but below) the half-integer value 3.5.

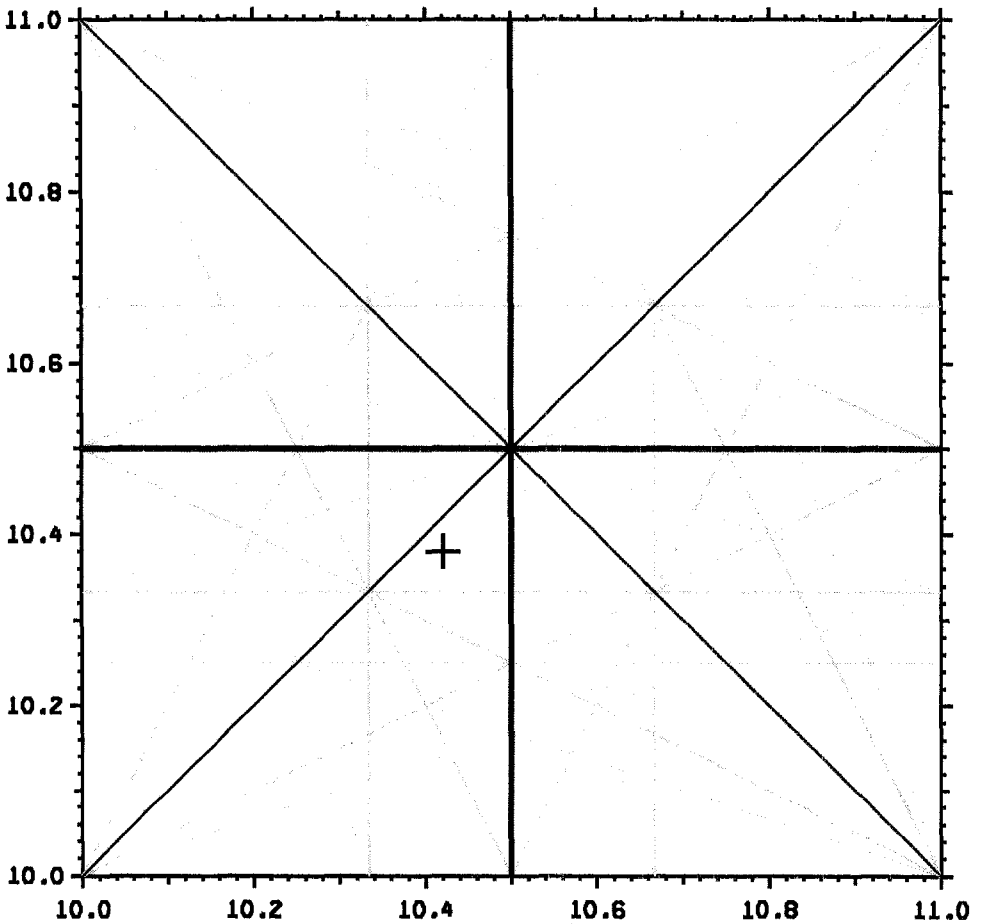

[Figure 8: Tune working point of the triangular lattice.]

Two families of chromaticity-correcting sextupoles can reduce the ring chromaticity to zero, but the ring will more likely be operated at a chromaticity of around -6 (1/3 the full natural value

Racetrack Lattice

The racetrack lattice (Figure 9) has essentially the same cell structure as the triangular lattice of Figure 6. It is only two cells (40 m) longer at 1360 m. It has the same number of dipoles (96) and 136 quadrupoles (1 m long.) The different layout allows for searies placement (for instance on top of a Los Alaoms mesa. It also allows a symmetric extraction scheme as will be discussed in the last chapter. γ_t for the racetrack lattice is slightly larger at about 9.4 (depending on the particular tune. The tune used in the figures are different from the ones used for the triangular lattice, but are Q_x = 10.90, Q_y =10.83. These tune provide better dispersion matching (see Figure 10,) but force us to operate in a busier region of phase-space (Figure 11.) From the point of view of dynamics the triangules lattice of Figure 7 is the best of the low-transition-gamma main rings. This is not a proble with injection at 8.5 to 9 GeV from the high-energy booster as discussed in the next chapter, but is direct inection at 800 MeV is required, then the lattice of Figure 7 is preferable.

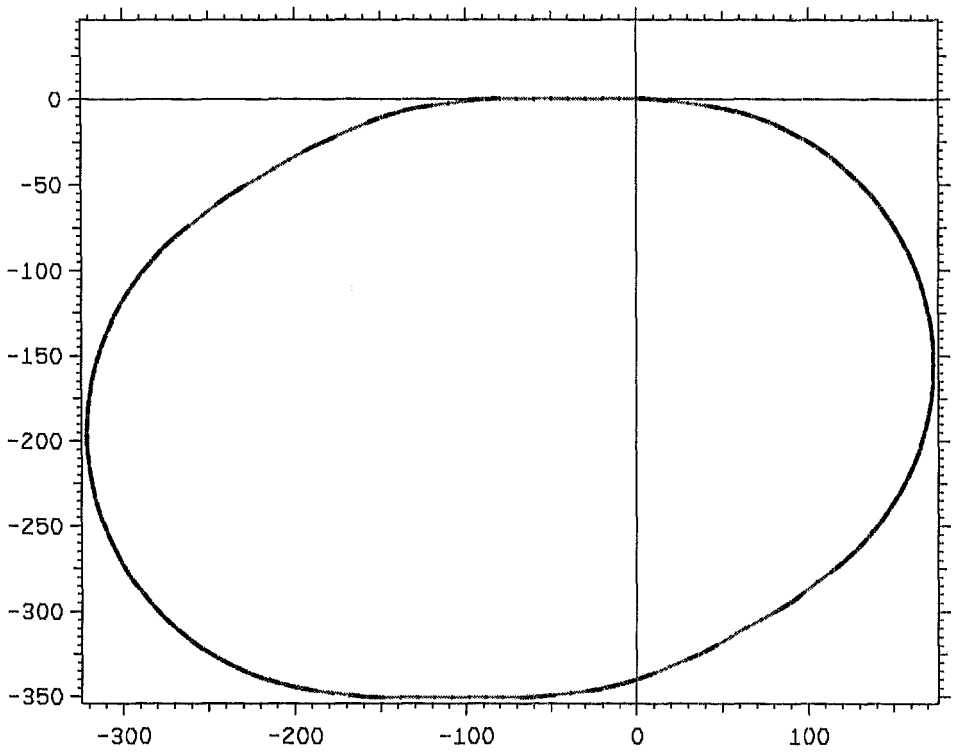

[Figure 9: Layout of the racetrack version of the low-transition-gamma 50 GeV main ring lattice.]

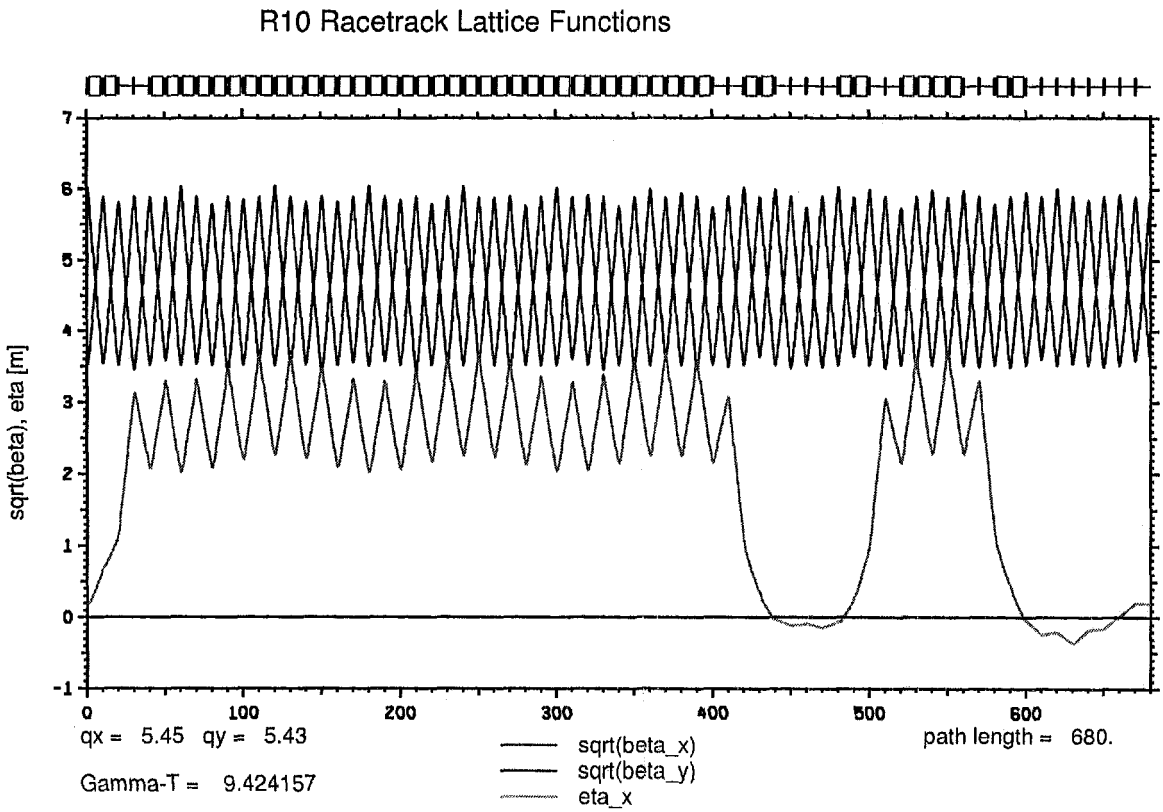

[Figure 10: Racetrack lattice functions in one superperiod (1/2 ring)]

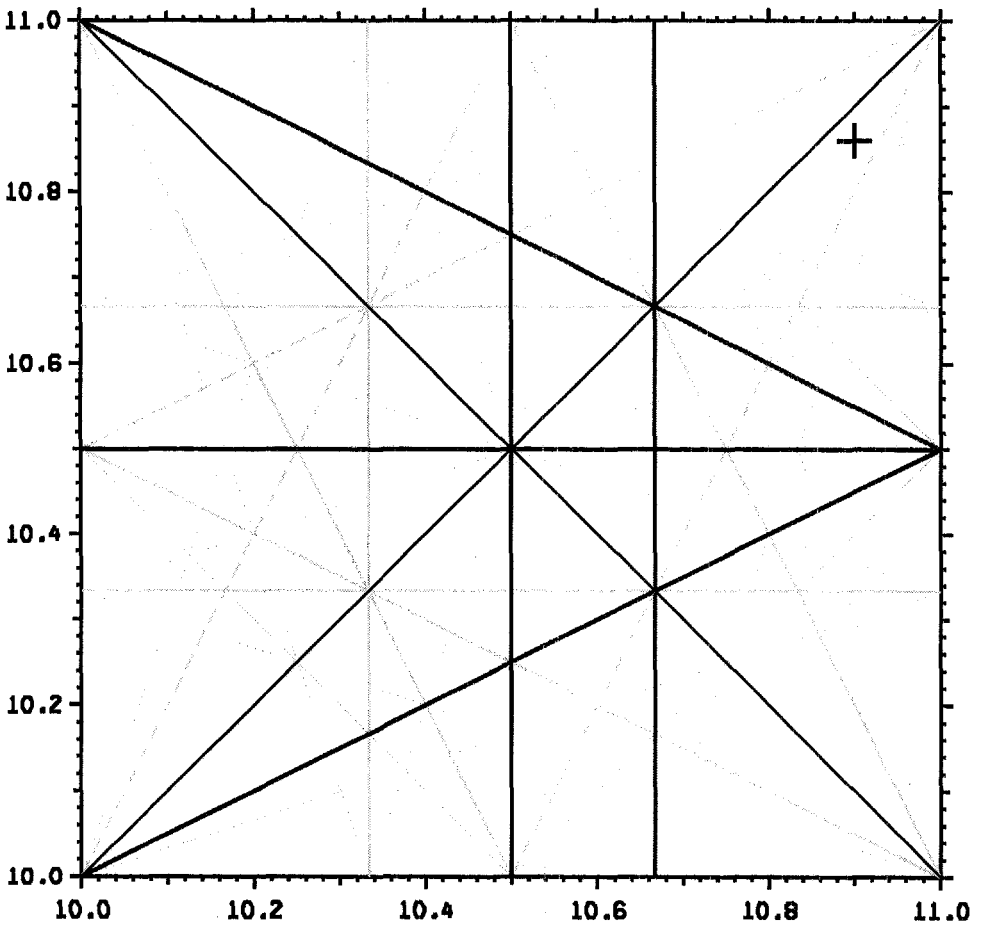

[Figure 11: Tune working point of the racetrack ring.]

New High-Energy Booster Lattice

The Booster ring shares many of the general design criteria of the Main ring lattice: robust conventional and conservative design, operational simplicity (few "knobs", few magnet types) and avoidance of transition crossing. The latter is readily achieved by simply raising the lattice γ_t above γ_{max}. Since the top energy is above 8 GeV, in a simplified lattice this requires a 90° phase-advance cell structure, with a missing-dipole superperiod. 16 identical superperiods (shown in Figure 2) make up the ring. Other design features include H^- strip injection from a linac at either 157 or 800 MeV, and acceleration of one or two bunches of 3-4 $x10^{12}$ protons at a 1 Hz cycle rate, a rate low enough to moderate RF power requirements. The booster will fill the main ring with 22 bunches in a period of 11 or 22 sec. The longer injection time is less of a problem at the higher extraction energy of the new booster (8.5 GeV.

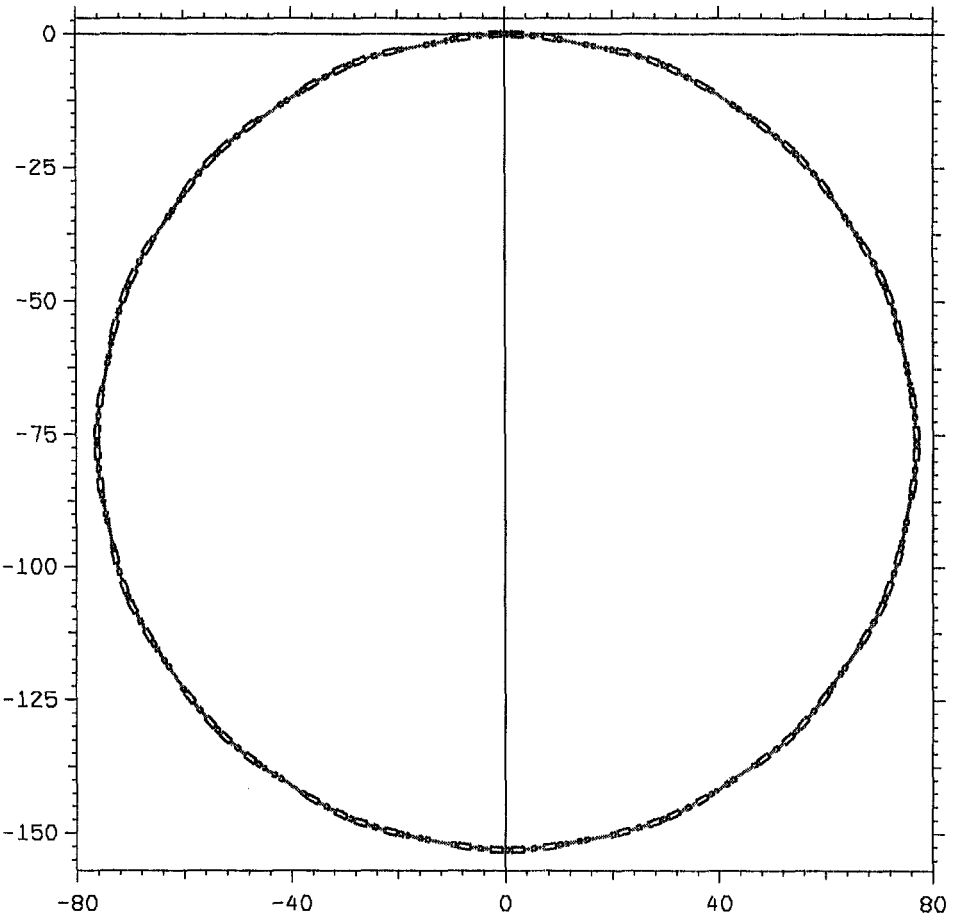

Figure 12. Layout of the high-energy booster ring lattice.

Figure 12 shows the layout of the revised, 16-sided Booster ring of 540 m circumference (85.94 m average radius). The lattice functions over one sector (superperiod), are shown in Figure 13, for a transition- γ_t of 13.87. This high, real γ_t value arises from the broad minimum in the dispersion function in the region of the bend dipoles. The phase advance of nearly 280° (nearly an odd multiple of 90°), is a positive aspect of this lattice design: the combination allows (1) convenient placement of injection bumpers to locally bump the circulating beam on/off the H^- stripping foil in the beam injection straight, and (2) efficient kick-extraction of the beam where a small-angle (3 mrad) fast kicker in one straight produces a sizeable (4 cm) beam displacement at an extraction septum magnet in the next straight. With injection hardware (bump magnets, H^- injection chicane magnets) placed in 3 successive sectors, extraction hardware (kicker, septum magnets) in 2 other successive sectors, and RF cavities in 4 more straights, 7 undedicated straights remain for other uses.

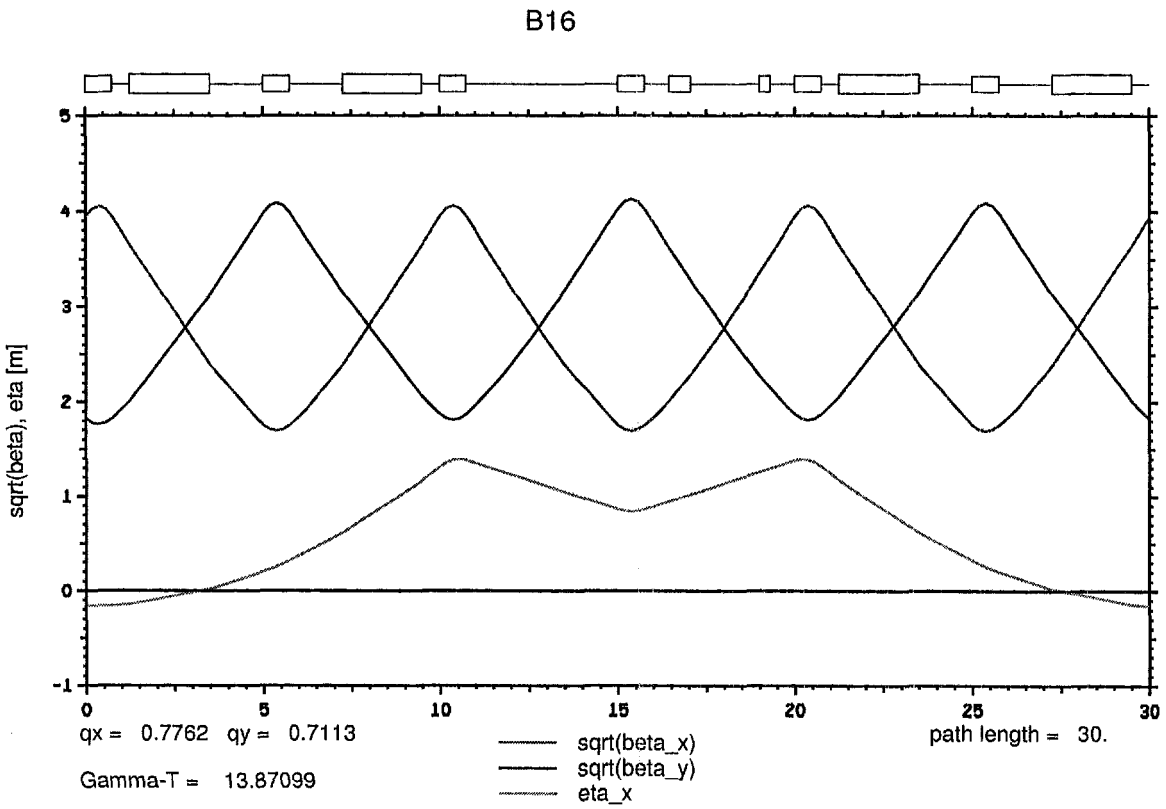

Figure 13. Booster lattice functions for one superperiod.

The maximum value of β_y in the dipoles is less than 10 m , allowing storage of the design emittance with dipole with a full gap of only 6 cm. The smaller dipole gap allows savings in the dipoles stored energy and weight, with respect to previous booster designs that had a β_y maximum in the dipoles of about 25 m. The betatron tunes for this Booster lattice are Q_x = 12.42, Q_y = 11.38. The choice of fractional tunes (0.42, 0.38) places the nominal working point in a region of betatron tune space largely free of systematic and structural sum resonances, as illustrated in Figure 3. Horizontal and vertical tune integers are widely split, so effects of the nearby octupole coupling resonance $2\upsilon_x - 2\upsilon_y = 2$ should be minor. Laslett coherent and incoherent space-charge tune shifts of order -0.15 at beam injection from a 157 MeV linac result in a diagonal bow-tie shaped tune spread region below this working point which encompasses several sextupole sum resonances (one normal, two skew), but preliminary beam simulations using the space-charge code SIMPSONS show no dramatic ill-effects at full intensity with high-quality quadrupoles.

Two families of short chromaticity-correcting short sextupoles (0.16 m long, 2 per sector) reduce the ring natural chromaticity from -20 to zero, if desired, with modest (0.1T) pole tip fields. More likely, the ring will be operated at about ⅓ this chromaticity value.

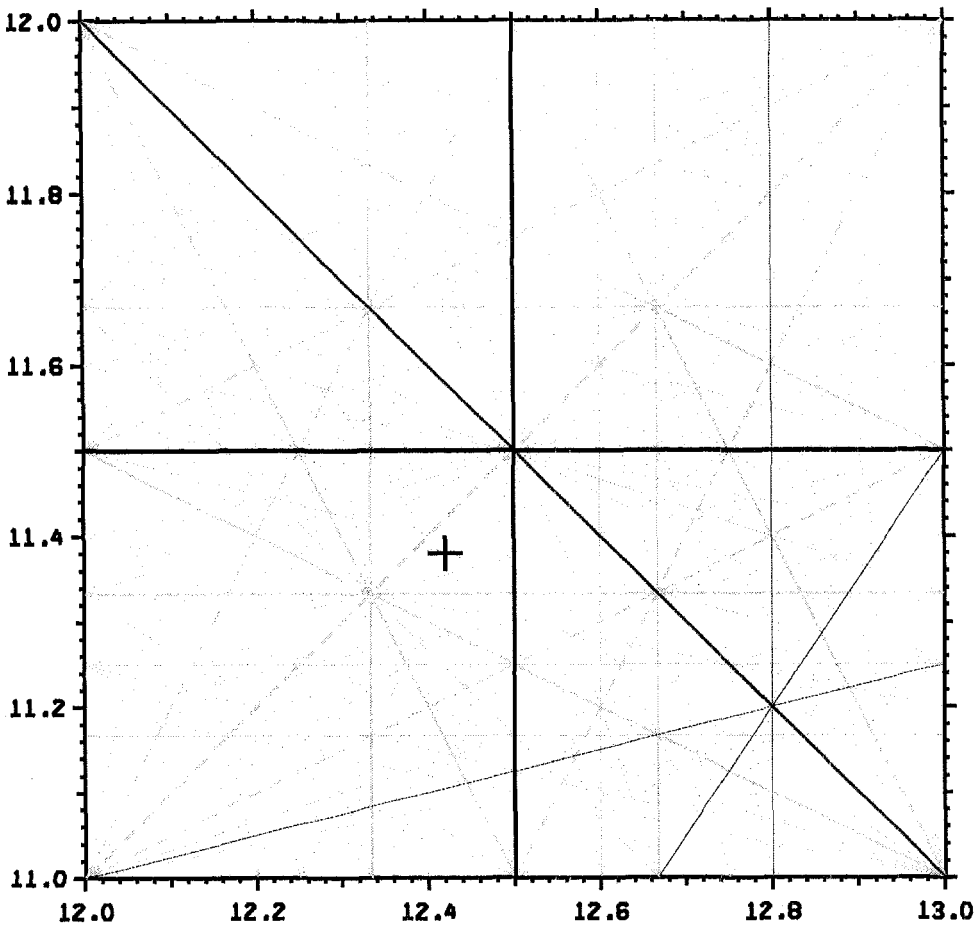

Figure 14: Booster tune diagram, showing low-order resonances
and nominal working point (cross.) Difference structural resonances are in color.

The Compact Dual-Extraction Layout

The long straight sections on either side of the main ring may both be used for beam extraction. This dual extraction layout offers some advantages over the previously described single extraction into a large transport system. The beam pulses are extracted simultaneously in pairs on both sides of the ring, and transported synchronously to the firing point. This provides twice as many protons per image as single extraction schemes, thus expending the total supply of pulses in the ring on half as many frames. A ring holding 20 pulses thereby provides a 10 frame movie, rather than a 20 frame one. Ten frames that are twice as bright is actually much closer to actual need than 20 dimmer frames. The dual extraction scheme requires an extra kicker, but saves the initial splitter used in the single extraction scheme. Pulse scheduling remains simple and flexible, requiring only that the same extraction pattern be applied to each half of the ring. Beam transport to the firing point is no longer synchronous by symmetry, but requires the solution of a pair of linear equations for the drift lengths and location of the firing point. The final part of our standard "Lobster" synchronous transport layout is substituted for part of the final straight sections leading

to the firing point. The orientation angle of the whole final transport system is a parameter of the design, but is only considered in multiples of the standard transport dipole bend angle of 3.75 degrees. The angle providing the shortest overall tunnel consistent with the length constraints is shown in the figure for a 12-view system. The entire system from linac to final lenses fits readily in a one kilometer square. An 8-view system looks very much the same, but fits in a square 5% smaller at 950 meters on a side, which means site considerations play little role in choosing between 8-view and 12-view systems. The main difference is that 8-view systems cost 50% less, and provide 50% better proton statistics from a given ring than 12-view systems, at the cost of worse tomographic performance. The 8-view system lenses could also be designed with somewhat better resolution due to reduced crowding around the firing point..